Hindawi
Shock and Vibration
Volume 2023, Article ID 6590979, 17 pages
https://doi.org/10.1155/2023/6590979

Research Article

Application of BP Neural Network Improved by Fireworks Algorithm on Suspender Damage Prediction of Long-Span Half-Through Arch Bridge

Jian Guo [1] **and Wu Guo** [2]

[1]*College of Architecture and Civil Engineering, Qiqihar University, Qiqihar 161000, China*
[2]*College of Communication and Electronic Engineering, Qiqihar University, Qiqihar 161000, China*

Correspondence should be addressed to Jian Guo; 332923661@qq.com

Received 28 March 2023; Revised 30 May 2023; Accepted 28 June 2023; Published 5 July 2023

Academic Editor: Denise-Penelope Kontoni

In recent decades, with the large-scale construction and rapid development of half-through arch bridges, as well as the increase of bridge service time, the suspender damage of arch bridge has become increasingly prominent. Therefore, real-time monitoring and regular detection of the health of arch bridge suspenders and timely detection and accurate judgment of the damage location and extent of suspenders are of great engineering significance for evaluating the reliability and residual life of arch bridge structures. By analyzing the main difficulties and existing problems of suspender damage identification, this paper takes the change rate of modal curvature as the damage index, introduces fireworks algorithm into the neural network model, optimizes the optimization process of neural network weight and threshold, and proposes a prediction model based on improved BP neural network by fireworks algorithm. According to the measured data of the damage degree of a long-span arch bridge in daily monitoring and on-site inspection, the proposed prediction method is applied to verify the effectiveness and accuracy in engineering health detection. On this basis, the improved BP neural network by fireworks algorithm is used to predict the suspender damage of a certain long-span half-through arch bridge, which provides an important basis for the actual bridge safety assessment.

1. Introduction

With the development of smart cities and the progress of science and technology, countries all over the world have increased their investment in infrastructure construction. A large number of complex structural forms have emerged, such as super-high-rise buildings, long-span spatial structures, super-large bridges, large dams, nuclear power plants, and large marine structures [1, 2]. These structural forms have brought great convenience to economic development and people's lives, but once damaged, they will do great harm to our cities. Large scale and complexity are the development direction of the structure, and its service life is often decades or even hundreds of years. In this service process, the structure will be damaged to varying degrees due to congenital defects such as design and construction, catastrophic factors such as external load, environmental factors, material aging, corrosion effect, fatigue effect, and other uncertain factors [3]. After the damage, the bearing capacity and durability of the structure will be affected, the ability to resist external forces will be significantly reduced, and then accidents will occur. This will lead to heavy casualties and economic losses and cause adverse social impact [4]. Taking the bridge structure as an example, the data statistics show that various deterioration phenomena occur on the bridge decks of about 253000 concrete bridges in the United States. Some of the bridges have been damaged in different forms and degrees in less than 20 years of service. Moreover, 35000 bridges will be added every year, and the average number of partially or completely collapsed bridges is about 200 every year. The construction cost of 11 concrete viaducts located on the ring expressway in the middle of

England Island is 28 million pounds. However, the maintenance cost reached over 120 million pounds, which will be close to six times the original cost. According to the Yangcheng Evening News in China, the Department of Communications of Guangdong Province organizes a large number of personnel to conduct a general survey on the technical status of existing and under-construction roads and bridges in the province. The results showed that of the 18700 bridges in Guangdong Province, 4244 were in category III and IV poor conditions and had insufficient bearing capacity, accounting for 22.7% of the total census, with a cumulative length of 109616 linear meters. For example, arch bridges have been widely used due to their beautiful appearance, simple construction methods, and strong spanning capacity. The suspenders of arch bridges in service commonly suffer from diseases, which directly affect the safety and durability of bridge structures. The suspender can be damaged or even broken due to corrosion, fatigue, and other reasons, which can greatly shorten the service life of the bridge and increase the risk of bridge collapse, as shown in Figure 1. Therefore, it is particularly important to identify the damage of bridge suspenders [5].

It can detect and predict the performance of the structure in real time, find and judge the damage location and degree of the structure in time, and then predict the performance change and remaining life of the structure to obtain the maintenance decision and the evacuation of local residents, which is of great significance to improve the service efficiency of engineering structures and ensure the safety of people's lives and property [6]. As the core of structural health monitoring, the successful research of damage identification has essential guiding significance for how to establish the health monitoring system of engineering structures. Therefore, the research on structural damage identification has become a hot issue in the field of structural health detection [7]. Structural damage detection technology and its identification methods have made great progress in academic or practical application research in recent years, but there are still many problems to be further studied and solved in the damage detection of complex civil engineering structures such as high-rise buildings and bridges [8]. A considerable part of the existing damage detection technologies and methods for civil engineering structures are copied from aerospace, aerospace, and mechanical structures. When the same technology and method are introduced into another discipline, we should pay attention to its applicability and the characteristics of this discipline.

At present, there are also some technical difficulties in the field of engineering structure damage detection [9]. Firstly, civil engineering structures are different from aviation, aerospace, and mechanical structures. Relatively large model error is allowed in design, analysis, and calculation. However, if a large error exists in the model used for detection, it will lead to a great difference between the calculated and actual dynamic characteristics of the damaged structure, so the error of the detection results based on the dynamic characteristics will be very large. Secondly, noise is unavoidable due to the influence of many

Figure 1: Bridge deck collapse due to boom breakage.

factors of the engineering structure. In the process of long-term health detection, noise may be introduced at every step and link from data acquisition to transmission. Therefore, a good ability to filter noise is what the identification method used should have. At present, damage identification in engineering structures is a nonunique problem, and if it cannot be well distinguished, it will result in unpredictable results of damage location and degree.

Because of the existence of these factors, many damage identification methods become invalid, which makes the research of damage identification face bottleneck. Therefore, a new method to overcome the above difficulties has become an urgent need [10–12]. The dynamic characteristics and response of the structure will change with the damage of the structure. In other words, there is a complex nonlinear relationship between the dynamic characteristics and response changes before and after the damage and the damage location and degree of the structure. The traditional acoustic emission method, ultrasonic method, infrared method, and other nondestructive testing techniques are not only time-consuming and expensive but also cannot detect some parts of large structures [13–15]. However, the dynamic characteristics and response of structures can be obtained through various detection methods and modal analysis. The artificial neural network (ANN) can take the damage index related to the dynamic characteristics and a certain response of the structure in various states as the input vector and take the damage diagnosis results (whether the damage exists, the damage location, damage degree, etc.) in various states as the output vector [16]. By learning to form a mapping, the neural network weights containing this mapping relationship can be saved, and there is no need to call the analysis model in the back analysis process. Through the effective and fast forward operation of the weight obtained by learning and the damage index obtained by detection, the damage diagnosis results can be obtained during the online diagnosis [17]. In a word, the achievements and research of artificial neural network in this field are still in the basic exploration stage, and it still needs the continuous efforts and exploration of relevant personnel to make the structural health monitoring technology and damage identification method better serve the field of engineering structures [18]. Since the performance of the neural network-based prediction model largely depends on the network structure and the weights and thresholds of each node of the network, the neural

network structure, initial weights, and thresholds of the network will greatly restrict the prediction accuracy and convergence of the neural network-based prediction model.

To sum up, aiming at the problem that the single neural network model has slow convergence speed and is easy to fall into local optimization, the existing research mainly focuses on the optimization and improvement of the neural network using intelligent optimization algorithms such as particle swarm optimization (PSO) and genetic algorithm (GA), which solves the problem of low prediction accuracy of the single neural network prediction model to a certain extent [19–23]. However, with the deepening of research, scholars found that the above algorithm itself also has aspects to be improved [24]. Improper setting of genetic operator will affect the search performance of the algorithm and make the algorithm easy to fall into local optimal solution [25], and too large initial population in PSO algorithm will lead to the problem of slow search speed of the algorithm, which will restrict the performance of optimizing BP neural network prediction model based on swarm intelligence algorithm [26]. For example, the BP neural network prediction model optimized based on GA algorithm is limited to the large sample data model, while the prediction ability of the sample model with small samples and uneven distribution is not significantly improved [27]. At the same time, the diversity of particles will be lost due to the too fast particle optimization speed, which restricts the accuracy of the prediction results of BP neural network model optimized based on PSO algorithm.

Fireworks algorithm (FWA) is a new swarm intelligence optimization algorithm proposed by Tan et al., which works by simulating the mechanism of simultaneous explosion and diffusion of firework at multiple points in the air [28]. It shows high optimization performance in solving optimization problems and has attracted the attention of scholars at home and abroad. Compared with GA and PSO algorithms, FWA simulates the mechanism of simultaneous explosion and diffusion of firework explosion operators and ensures the diversity of firework population; at the same time, the fireworks algorithm has stronger global search ability by introducing the idea of immune concentration and the distributed information sharing mechanism. Therefore, this paper introduces the fireworks algorithm (FWA) into the BP neural network model to optimize the weight and threshold of BP neural network, proposes a prediction model based on the fireworks algorithm to improve BP neural network (FWA-BPNN), to solve the problem that the traditional BP neural network prediction model has slow convergence speed and is easy to fall into the local optimal solution in the training process, and applies it to the damage prediction of long-span arch bridges.

2. Classical Model of BP Neural Network

BP neural network shows good self-learning and self-adjusting ability in solving nonlinear problems and is widely used to solve complex system prediction problems with many factors interlaced. The essence of the BP neural network prediction model is to train the model through a large number of data in the finite solution space and then find the weight w_{ij} and threshold between network neurons θ_i and other parameters to establish the mapping relationship between input and output and minimize the network error, as follows:

① Initialize the network weights and thresholds: the initial weights and thresholds of the network are initialized randomly in the interval [1, 1].

② Feed forward calculation: assuming that the weight value $w_{ij}^{(l)}(k)$ of the network in the kth iteration process, the threshold value $\theta_i^{(l)}(k)$ of the ith neuron, and the expected output $t_i(k)$ of the ith neuron node in the lth layer are known, then

$$\begin{cases} V_i^{(l)}(k) = \sum_{j=1}^{S^{l-1}} w_{\mathrm{ij}}^{(l)}(k) y_j^{(l-1)}(k) + \theta_i^{(l)}(k), \\ y_i^{(l)}(k) = f_l\left(V_i^{(l)}(k)\right), \end{cases} \tag{1}$$

where $V_i^{(l)}(k)$ is the input of the ith neuron in the lth layer of the neural network; $y_i^{(l)}(k)$ is the output of the lth layer; l is the layer number of the network and $l = 1, 2, \ldots L$; $1 \le i \le S^L$; and $y^{(0)}(k) = x(k)$.

③ Error backpropagation: calculate the error $\delta_i^{(l)}(k)$ of the lth layer in the kth iteration of the neural network through equations (2) and (3).

$$\delta_i^{(L)}(k) = -2\left(t_i(k) - f_L\left(V_i^{(L)}(k)\right)\right) f_L^{'}\left(V_i^{(L)}(k)\right), \tag{2}$$

where $t_i(k)$ is the expected output value of the ith neuron node, and $1 \le i \le m = S^l$. Based on this, $\delta_i^{(l)}(k)$ can be calculated by recursion formula (2) and $l = L-1, L-2, \ldots, 1$.

$$\delta_i^{(l)}(k) = \sum_{j=1}^{S^{l+1}} w_{\mathrm{ji}}^{(l+1)}(k) f_l^{'}\left(V_i^{(l)}(k)\right) \delta_j^{(l+1)}(k). \tag{3}$$

④ Update network weights and thresholds: use equation (4) to update the weights and thresholds of the neural network.

$$\begin{cases} w_{\mathrm{ij}}^{(l)}(k+1) = w_{\mathrm{ij}}^{(l)}(k) - \alpha \delta_i^{(l)}(k) y_j^{(l-1)}(k), \\ \theta_i^{(l)}(k+1) = \theta_i^{(l)}(k) - \alpha \delta_i^{(l)}(k), \end{cases} \tag{4}$$

where $w_{ij}^{(l)}(k+1)$ and $\theta_i^{(l)}(k+1)$ are the weights and thresholds of the network in the $k+1$ iteration process, respectively; α is the momentum factor; $1 \le i \le S^l$; $1 \le j \le S^{l-1}$; and $1 \le l \le L$.

3. Suspender Damage Prediction Model Based on Improved BP Neural Network with Fireworks Algorithm

3.1. Fireworks Algorithm. Fireworks algorithm is a new swarm intelligence optimization algorithm. For the optimization problem min $f(x) \in R$, $x \in \Omega$, to be solved, fireworks algorithm is used to solve the optimization problem. The specific steps are as follows:

① Initialize the population: Some fireworks are randomly generated in a specific solution space. Each firework individual x_i represents a solution in the solution space, that is, $x_i \in \Omega$.

② Calculate the fitness value: for each firework individual x_i in the initial population, calculate the fitness value $f(x_i)$ according to the fitness function $f(x)$ and calculate the number of fireworks produced by each firework explosion S_i and the explosion radius A_i according to the following equations:

$$S_i = c \times \frac{y_{\max} - f(x_i) + \varepsilon}{\sum_{i=1}^{N} (y_{\max} - f(x_i)) + \varepsilon}, \tag{5}$$

$$A_i = d \times \frac{f(x_i) - y_{\min} + \varepsilon}{\sum_{i=1}^{N} (f(x_i) - y_{\min}) + \varepsilon}, \tag{6}$$

where $y_{\max} = \max(f(x_i))$ $(i = 1, 2, \ldots, n)$ is the fitness value of the individual with the worst fitness value of all fireworks in the current population; $y_{\min} = \min(f(x_i))$ $(i = 1, 2, \ldots, n)$ is the fitness value of the best individual in the current population; c and d are constants, which are, respectively, used to limit the total number of sparks and represent the maximum explosion radius; and ε is a constant used to avoid the denominator being zero.

③ Generate sparks: Randomly select z dimensions to form a set Z, where $z = \text{rand}(1, d \times \text{rand}(0, R_i))$, and rand $(0, R_i)$ is a random number generated within the explosion radius A_i. In set Z, for each dimension k, use equations (7) and (8) to perform explosion mutation on fireworks, map sparks beyond the boundary through the Gaussian mutation mapping rules in equation (9), and save them in the spark population.

$$h = A_i \times rand(1, -1), \tag{7}$$

$$cx_{ij} = x_{\text{ij}} + h, \tag{8}$$

$$cx_{\text{ik}} = x_{\text{ik}} \times r, \tag{9}$$

where A_i is the explosion radius of the ith firework; h is the position offset; x_{ik} is the kth dimension of the ith firework in the population; ex_{ik} is the spark generated by the explosion of the ith firework; cx_{ik} is the Gaussian variation spark of x_{ik} after Gaussian variation; and r follows the Gaussian distribution.

④ Select the next generation group: The next generation firework population is selected by using the selection strategy, that is, N firework individuals are selected from the firework explosion sparks and Gaussian variation spark populations to form the next generation candidate firework population. For the candidate firework population K, the selection strategy is as follows: select the individual x_k with the minimum fitness value min $(f(x_i))$ as the next generation of firework population individuals directly, and the remaining $N - 1$ firework individuals adopt the roulette gambling method. For the candidate individual x_i, the probability formula (10) is adopted for its selection.

$$p(x_i) = \frac{R(x_i)}{\sum_{j \in K} R(x_j)}, \tag{10}$$

where $R(x_i)$ is the sum of the distances between firework individual x_i and other individuals, which is calculated by the following formula:

$$R(x_i) = \sum_{j=1}^{K} d(x_i, x_j) = \sum_{j=1}^{K} \|x_i - x_j\|. \tag{11}$$

⑤ Determine termination conditions: if the termination conditions are met, stop the iteration; otherwise, continue with step ②.

3.2. Improved BP Neural Network Prediction Model Using Fireworks Algorithm for Suspender Damage. The weight and threshold of BP neural network are the key factors, which affect the prediction performance of the BP neural network model. Therefore, the fireworks algorithm is introduced into the neural network model, and the position x_{ik} of firework individuals in the firework population is used to represent the weight coefficient of network nodes and the threshold of network neurons. Based on the above rules, the specific improvement strategies are as follows:

① Key parameter code: because the weights, thresholds, and firework individuals in the neural network are composed of a series of vectors, the real vector coding strategy is selected to code the key parameters in the model.

Note that $X = [x_1, x_2, \ldots, x_D]$ represents a set of parameters to be optimized, in which each dimension is composed of network weights and thresholds. In the neural network, note $n_{IW(1,1)}$ as the number of weight values between the input layer and the hidden layer, $n_{b(1,1)}$ as the number of neuron thresholds in the hidden layer, $n_{IW(2,1)}$ as the number of weights between the hidden layer and the output layer, and $n_{b(2,1)}$ as the number of neuron thresholds in the output layer; then, $D = n_{IW(1,1)} + n_{b(1,1)} + n_{IW(2,1)} + n_{b(2,1)}$.

② Calculate the fitness value: Initialize weight coefficient and threshold. Initialize the weight coefficient and threshold between nodes in the neural network in the interval [−1, 1], i.e., $x_i \sim U[-1, 1]$, and use the position of firework individual x_i in the fireworks algorithm to represent the weight coefficient of network nodes and the threshold of neurons, and then each firework individual represents a neuron in the neural network model.

③ Select the fitness function: The goal of algorithm model training is to make the network output layer result as close as possible to the expected result through continuous iterative calculation, to obtain the weight parameter $w_{ij}^{(l)}(k)$ and threshold value θ_{i} between nodes when the network output result is optimal. In the FWA-BP neural network, the square error function is introduced to calculate the fitness value of individual fireworks.

$$\mathrm{SSE} = \sum_{p=1}^{P} \sum_{t=1}^{S} (t - y)^2, \tag{12}$$

where t is the expected output of the network; P is the number of layers of the network; S is the number of network output units; and y is the actual output value of the network.

The actual output value of the network is specifically expressed in the following equation:

$$y_i = f_i\left(\sum_{j=1}^{n} w_{\mathrm{ij}} x_j + \theta_i\right), \tag{13}$$

where x_j is the input of the network; $w_{ij}$is the weight of network nodes; θ_i is the threshold value of the ith neuron in the network; and $\theta_i = -w_i(n+1)$.

The fitness function $f_i(x)$ is given in the following equation:

$$f_i(x) = \sum_{p=1}^{p} \sum_{t=1}^{s} (t - y)^2 = \sum_{p=1}^{p} \sum_{t=1}^{s} \left(t - f_i\left(\sum_{j=1}^{n} w_{\mathrm{ij}} x_j + \theta_i\right)\right)^2. \tag{14}$$

④ Optimize firework population: For each firework individual x, calculate its fitness value $f(x_i)$ with equation (14), and calculate the number of explosive fireworks S_i and explosion radius A_i with equations (5) and (6). At the same time, based on equations (7)–(9), each firework individual is operated with explosion, displacement, and mutation, and the selection strategy of equations (10) and (11) is used to select the best firework individual to form the next generation of firework population.

⑤ Determine termination conditions: According to equations (11) and (14), calculate the fitness value $f(x_i)$ of the firework individuals in the firework population and the Euclidean distance $R(x_i)$ between the firework individuals and judge whether the termination condition of the maximum number of iterations is satisfied. If it is satisfied, the new firework population is composed of the firework individuals with the minimum fitness value min $(f(x_i))$ and the firework individuals with the maximum distance max $(R(x_i))$ in the current firework population, and take the current firework population as the optimal firework population X_{best}; otherwise, continue with step ⑤.

⑥ Update network weights and thresholds: Use the optimal firework population X_{best} obtained in step ⑤ to initialize and update the weight and threshold vector X in the network model. Based on the above steps, the flowchart of the whole FWA-BP algorithm can be obtained, as shown in Figure 2.

4. Health Inspection Analysis of Long-Span Arch Bridge

4.1. Health Inspection of the Long-Span Arch Bridge. To verify the validity of the prediction model based on FWA-BP neural network, the damage detection and experimental data of a long-span arch bridge are selected, and the prediction model based on FWA-BP neural network is experimentally verified and compared. The research object of the arch bridge used in this paper is shown in Figure 3. The bridge site of this bridge has a water surface width of about 230 m, a deep water flow, a minimum elevation of −36.57 m at the trough bottom, and a maximum navigable water level of 5.9 m. The rock on the bank is exposed, and the elevation of the north south small mountain top is about 27.00 m. The elevation of the foot of the mountain is about 6.00 m, and the surface of the mountain is covered by the Quaternary eluvial layer, with the surface rock mass in a gravel shape. The main bridge is a through steel tube concrete ribbed arch bridge with a main span of 245 m. The arch axis is a quadratic parabola, with a rise span ratio of 1/5, a rise height of 49 m, and a bridge deck width of 22.5 m. Among them, the carriageway is 15 m wide, the sidewalk is 2 ∗ 1.5 m wide, and the design load is Grade 20 for automobiles, the trailer weighs 100 tons. The distance between suspenders is 5.9 m, and double suspenders are used. The main arch of the steel pipe arch hoisting bridge weighs from 53 to 61 tons per section, and the entire bridge has 27 installation sections, with a total weight of 1220 tons.

The arch ribs are concrete filled steel tubular trusses of equal height and width, and the upper and lower chords are of flat dumbbell shaped sections. Paired vertical web members and diagonal members are set between the upper and lower chords, which are, respectively, directly connected to the circular tubes of the chords. The total height of the arch rib section is 4.4 m, and the total width is 1.9 m. Within the range of 16.766 m above the arch springing line of the arch foot, the truss structure is wrapped with No. 50 reinforced concrete to form a reinforced concrete box rib section with a height of 4.8 m and a width of 2.3 m. Shear keys are added to the wrapped section and reinforcement is adjusted. The main pipes, batten plates, web members, and

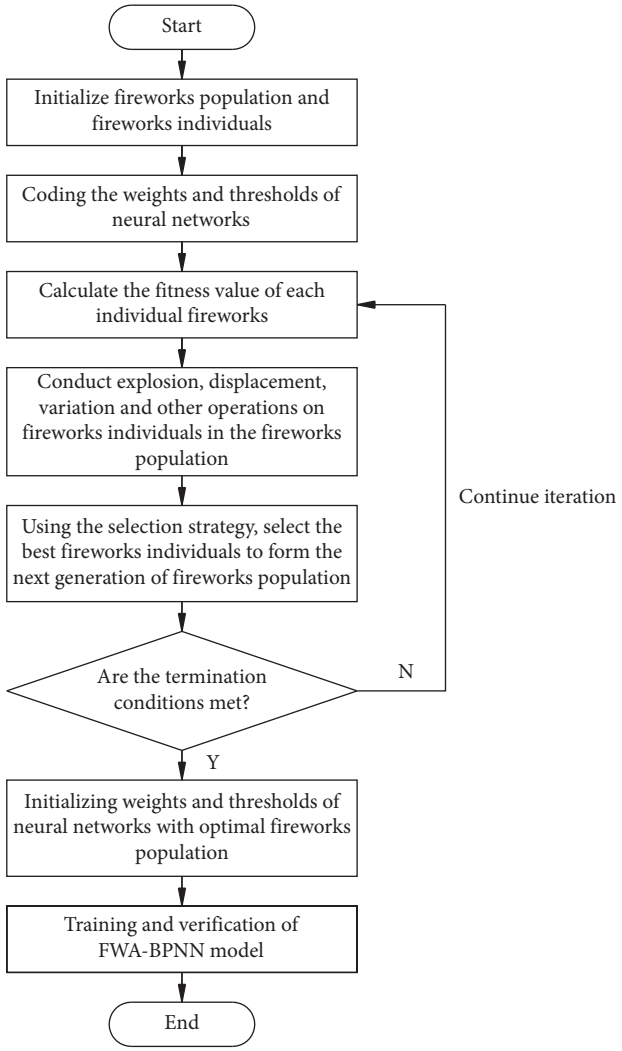

Figure 2: The flow diagram of the improved BP neural network with fireworks algorithm.

Figure 3: Schematic of the research arch bridge in this paper.

transverse joints of the upper and lower chords of the arch rib are made of 16 Mn steel, the main pipes are made of spiral welded pipes, and the web members are made of seamless steel pipes. The main pipe and batten plate cavities of the upper and lower chords are filled with C50 micro-expansive concrete. A total of 7 spatial steel pipe cross braces are provided for the entire bridge, including 5 above the bridge deck and 2 below the bridge deck. The cross bracing of the arch crown adopts a meter shaped lattice structure, and the rest adopts a straight shaped lattice structure.

The bridge deck system consists of 41 cast-in-situ sections and 38 prefabricated beams, and continuous bridge decks are formed between adjacent beams through cast-in-situ flange joints. Prefabricated beams are divided into upper column beams and suspender beams, both of which are prestressed concrete open box girders. The bridge deck of the column beam and suspender beam on the arch is a simply supported structure, which releases the temperature change and shrinkage and creep displacement of the entire continuous bridge deck system structure through the expansion joints at the simply supported ends. A box shaped steel beam is provided at the intersection of the bridge deck system and the arch ribs, with a total of two sets for the entire bridge. The bridge deck is paved with 9 cm thick steel fiber concrete and 4 cm thick asphalt concrete. The bridge deck adopts a 3% two-way longitudinal slope and a 1.5% two-way transverse slope. The longitudinal slope of the bridge deck is adjusted by the inclination of the beam flange plate, and the transverse slope is adjusted by the height change of the beam.

In order to improve stability, column top tie beams have been added to No. 1 and No. 2 columns with column heights exceeding 8 m above the arch. Each suspender beam is equipped with double suspenders with a spacing of 1.5 m, and the suspension rod is composed of 55 galvanized high-strength steel wires with a diameter of 5mm, and the outer layer is protected by hot extruded polyethylene. Both ends are cold casting heading anchorage. To avoid direct exposure to the atmosphere, the upper and lower anchor heads are protected by protective covers. To protect the exposed steel wire (approximately 50 cm long) near the anchor head under the suspender, cement mortar is poured into the conduit under the suspender. At the same time, the suspender is wrapped with stainless steel within 3 m above the bridge deck to avoid man-made damage.

The vertical web, diagonal web, and lateral connection systems of this bridge adopt hollow steel tube structures that are not filled with concrete. The inner surface of the empty pipe structure is required to be sealed and coated with two layers of rust-resistant paint. The anti-corrosion treatment of the outer surface of the steel structure adopts the GCM polymer material protection system. There are two forms of anti-corrosion for the outer surface of the arch foot outer covering section structure: the surface in contact with the concrete (including the batten plate) is not subject to anti-corrosion treatment, the shear key is welded, and rust removal treatment is conducted to ensure a good combination with the concrete. The surface of the exposed part also adopts a GCM polymer material protection system.

4.2. Suspender Damage Experimental Analysis of the Long-Span Arch Bridge. The bridge is a key transportation hub connecting the north and south sides, with an average of more than 12000 vehicles passing through it every day. Since its completion and opening to traffic, it has been operating

for a long time, so long-term and comprehensive health testing and related scientific experiments have been conducted on the bridge.

The outer surface of the arch rib steel structure adopts a GCM polymer material protection system. Upon inspection, it was found that the anti-corrosion coating surface of the steel pipe arch rib has anti-rust phenomenon, with severe peeling and peeling in some parts and cracks in some parts. There are cracks on the concrete surface wrapped around the arch rib, mainly along the arch axis and perpendicular to the arch axis. In addition, there are a small number of oblique cracks, and a small number of cracks are accompanied by bleeding phenomenon.

There are 120 suspenders in the whole bridge, all of which are high-strength steel wire bundles. Except for the eight suspenders whose upper anchor heads are anchored in the upper chord batten concrete, the remaining suspenders' upper anchor heads are all anchored in the lower chord batten concrete, and the anchor heads are all cold casting heading anchorage. Upon inspection of the protective cover, it was found that the anti-corrosion coating of the anchor head protective cover had pitting and spot corrosion, and in severe cases, there were peeling and peeling phenomena, as well as the lack of fixing bolts. The statistical results of the diseases of the upper anchor head protective cover are shown in Table 1.

For the inspection of anchor heads, 16 anchor heads are selected from both upstream and downstream sides at the upper end for inspection, while the first anchor head from both upstream and downstream sides and the midspan anchor head are selected for inspection at the lower end. Upon inspection, it was found that there was condensed water on the inner wall of the protective cover and the top of the anchor cup cover, there was rust on the outer side of the anchor cup, the butter in the anchor cup had dried and evaporated, and the steel wire pier head was exposed and corroded. The inspection results of anchor head corrosion are shown in Table 2. For ease of expression, the anchor heads are numbered sequentially from south to north. The upstream, downstream, and upper and lower ends are distinguished by UT, UB, DT, and DB. For example, UB2 represents the second lower anchor head on the upstream side, and so on.

As can be seen from Table 2, most of the upper and lower anchor head protective covers have condensed water. When there is no or a small amount of accumulated water inside the anchor cup of the upper anchor head, the steel wire pier head may experience whitening. When there is a large amount of accumulated water, the steel wire pier head will produce slight rust. The corrosion condition of the suspender was inspected, and some suspenders were selected to inspect the cable body under the protection of the intermediate PE pipe. It was found that the suspender cable body was not corroded. After the inspection, the cable body is sealed with cellophane and epoxy resin.

The surface of the precast beam concrete for the bridge deck system is uniform in color, and there are no cracks, peeling, and exposed reinforcement. However, there are alkalization and whitening phenomena on the local concrete surface. The cast-in-place concrete has cracks, mainly longitudinal cracks. Some cracks exceed the limit in width, with a maximum of 0.41 mm. In addition, there are a few oblique cracks. The bridge deck pavement shall be free of looseness, oil spillage, cracking, waves, ruts, pits, and subsidence. Most expansion joints are blocked by foreign objects and lose their expansion function. The measurement of bridge geometry includes the measurement of bridge deck geometry and arch axis geometry, which is arranged during the period when the structural temperature tends to stabilize.

The bridge deck alignment measurement is conducted using a precision electronic level combined with an indium steel ruler. Under the condition of closing all traffic on the bridge deck, it is divided into two zones, upstream and downstream, for round-trip closed leveling. The measuring points are arranged at the eighth point of the bridge deck. The permanent measurement is arranged inside the collision barrier of the upstream and downstream side traffic lanes. Comparing the design value and the measured value of the bridge deck alignment, it is found that the overall bridge deck alignment has decreased, with the difference between the measured value and the design value being between −0.095 m and 0.069 m.

The arch axis is measured using a tunnel section detector. Due to site conditions, only the arch axis elevation within 68.6 m from the midspan was tested and compared with the design value. It was found that the measured arch rib alignment slightly changed compared to the design alignment, with a difference between −0.015 m and 0.094 m. According to the theory of string vibration, the cable force of the suspension rod of the entire bridge is measured using a dynamic cable force tester.

When measuring the natural vibration frequency of the suspension rod of the bridge using the vibration frequency method, two sets of equipment, a dynamic signal collector and a cable force tester, are used together. When using a dynamic signal collector, fix the acceleration sensor with black electrical tape at half of the suspension rod, connect the dynamic signal collector through the sensor cable, and synchronize the collector with the computer acquisition system. Then, collect the natural frequency of the suspension rod under both environmental and manual excitation. For the bridge site during the operation period, environmental random vibration is selected, and the suspension rod is directly excited by using vehicle loads and wind loads in the environment as the vibration sources of the suspension rod. During measurement, if the suspension rod is stationary and there is no natural vibration or the measured natural vibration frequency is unclear, a certain amount of artificial excitation is required for the suspension rod. A small wooden mallet is used to strike the suspension rod as artificial excitation, which can compensate for the unstable and weak environmental vibration source.

The random vibration of the environment is tested using a cable force dynamic tester. The cable force dynamic tester is a portable single or dual-channel vibration detection analyzer for micro-vibration signals. The accelerometer is fixed on the suspension rod to measure its lateral vibration. The cable force dynamic tester can collect the multi-

Table 1: Statistics on diseases of upper anchor head protective cover.

Number of upper anchor heads (pcs.)	Pitting corrosion		Peeling		Missing bolts	
	Quantity (pcs.)	Percentage (%)	Quantity (pcs.)	Percentage (%)	Quantity (pcs.)	Percentage (%)
120	39	32.5	28	23.3	61	50.8

harmonic vibration curve of the suspension rod and obtain the lateral vibration frequency of the suspension rod through spectral analysis. The characteristic of the corresponding relationship between the cable force and the vibration frequency of the cable is utilized. When the length of the cable, the constraint conditions at both ends, and the distribution mass are known, the cable force of the suspension rod of the bridge can be obtained by measuring the vibration frequency of the cable.

In order to reduce measurement errors, the test points of the same suspension rod will be selected at different heights for multiple measurements under time constraints, and the measured natural frequencies will be compared to avoid significant errors in the data. In Table 3, the comparison between the tested cable force results and the cable force at completion acceptance. For ease of expression, the suspenders are numbered sequentially from south to north, and the upstream and downstream are distinguished by U and D. The first upstream suspender on the south side is U1, the first downstream suspender is D1, the first upstream suspender on the north side is U60, the first downstream suspender is D60, and so on.

In Table 3, the difference value = the measured value of regular inspection – the measured value of handover acceptance. The difference value is positive when the cable force increases and negative when the cable force decreases. From Table 3, it can be seen that the cable force of the suspender tested this time is generally deviated from the cable force at the completion acceptance, with most of the difference between 10 kN and 40 kN, with a maximum difference of 106.2 kN.

5. Damage Prediction Calculation Based on FWA-BP Neural Network Prediction Model

5.1. Suspender Damage Prediction Modeling of Arch Bridge. Using the FWA-BP neural network prediction model and taking the damage prediction of long-span arch bridge suspenders as an example, the damage prediction model based on FWA-BP neural network is established. The steps are as follows:

① Select the input and output indicators: ten indexes, such as modal curvature change rate, elastic modulus, frequency, vibration mode, boom damage location, noise level, instantaneous bearing weight, lateral bending vibration displacement, beam linear mass, and bending stiffness, are selected as the input indexes of the network prediction model, and the boom damage degree is selected as the output index of the network prediction model.

② Standardize the data: To eliminate the impact of different dimensions on the accuracy of the prediction model, standardize the data for each indicator to the same order of magnitude, to improve the comparability between the data. This model adopts 0-1 standardization method to standardize the experimental data.

$$X^* = \frac{x_k - \min(X)}{\max(X) - \min(X)}, \tag{15}$$

where max (X) is the maximum value in the dataset and min (X) is the minimum value in the dataset. After the data are standardized, the training data are mapped to the interval [0, 1] for comparative analysis.

③ Set key parameters: on the basis of the input and output indexes of the prediction model, the main parameters based on FWA-BP neural network are set as follows—the number of nodes in the input layer $m = 10$, the number of nodes in the output layer $n = 1$, the number of hidden layers $e = 1$, and the number of neurons in the hidden layer s of the neural network, and then empirical formula (16) is used to calculate $s \approx 6$.

$$s = \sqrt{0.43mn + 0.12n^2 + 2.54m + 0.77n + 0.35} + 0.51 \approx 6. \tag{16}$$

For the selection of activation function, *tansig* and *purelin* activation functions are selected in the input layer and output layer, respectively, and *trainlm* function is selected as the training function of the network model. In the process of network training, set the learning rate as 0.01, the momentum factor as 0.9, the maximum number of iterations as 20000, and the minimum training error as 0.001. For the weight value w_{ij} and threshold between network nodes θ, the optimal firework population obtained by iterative selection of fireworks algorithm is used to initialize the network weight and threshold.

Table 2: Corrosion condition of anchor head.

Anchor head number		Damage type				
		Condensation inside the protective cover and on the top of the anchor cup cover	Water accumulation in anchor cup	Rust degree of anchor cup	Volatility of butter	Rust degree of steel wire pier head
Upstream upper anchor head	UT3	Not have	Not have	Mild	Serious	Whitening
	UT4	Have	Many	Mild	Serious	Mild
	UT7	Have	Many	Mild	Serious	Mild
	UT8	Not have	Not have	Mild	Serious	Whitening
	UT10	Have	Many	Mild	Serious	Mild
	UT14	Have	Many	Mild	Serious	Mild
	UT20	Have	Few	Mild	Serious	Whitening
	UT26	Have	Many	Mild	Serious	Mild
	UT30	Have	Many	Mild	Serious	Mild
	UT38	Have	Few	Mild	Serious	Whitening
	UT41	Have	Many	Mild	Serious	Mild
	UT46	Have	Many	Mild	Serious	Mild
	UT47	Not have	Not have	Mild	Serious	Whitening
	UT51	Have	Many	Mild	Serious	Mild
	UT54	Not have	Not have	Mild	Serious	Whitening
	UT59	Not have	Not have	Mild	Serious	Whitening
Downstream upper anchor head	DT3	Not have	Not have	Mild	Serious	Whitening
	DT4	Have	Many	Mild	Serious	Mild
	DT6	Not have	Not have	Mild	Serious	Whitening
	DT10	Not have	Not have	Mild	Serious	Whitening
	DT14	Have	Few	Mild	Serious	Whitening
	DT20	Have	Few	Mild	Serious	Whitening
	DT21	Have	Many	Mild	Serious	Mild
	DT27	Have	Many	Mild	Serious	Mild
	DT31	Have	Many	Mild	Serious	Mild
	DT36	Have	Many	Mild	Serious	Mild
	DT40	Have	Many	Mild	Serious	Mild
	DT44	Have	Many	Mild	Serious	Mild
	DT48	Have	Few	Mild	Serious	Whitening
	DT51	Not have	Not have	Mild	Serious	Whitening
	DT55	Not have	Not have	Mild	Serious	Whitening
	DT58	Have	Many	Mild	Serious	Mild
Upstream lower anchor head	UB1	Not have	Not have	Mild	Serious	Whitening
	UB30	Have	Many	Mild	Serious	Mild
	UB60	Have	Few	Mild	Serious	Whitening
Downstream lower anchor head	DB1	Have	Not have	Mild	Serious	Whitening
	DB30	Have	Many	Mild	Serious	Mild
	DB60	Have	Few	Mild	Serious	Whitening

Table 3: Test results of dead load cable force (unit: kN).

Boom no.	Regularly detected measured value	Actual value of handover acceptance	D value	Boom no.	Regularly detected measured value	Actual value of handover acceptance	D value
U1	369.4	351.7	17.7	D1	361.1	346.3	14.8
U2	422.6	408.4	14.2	D2	378.9	363.5	15.4
U3	391.3	372.5	18.8	D3	382.6	366.1	16.5
U4	370.5	368.2	2.3	D4	366.1	359.4	6.7
U5	403.9	387.5	16.4	D5	385.8	373.5	12.3
U6	367.4	351.5	15.9	D6	359.8	346.2	13.6
U7	492.3	475.1	17.2	D7	429.7	413.4	16.3
U8	291.6	277.3	14.3	D8	336.3	320.5	15.8
U9	416.1	398.3	17.8	D9	410.3	394.5	15.8
U10	371.3	349.6	21.7	D10	347.5	329.7	17.8
U11	388.5	368.7	19.3	D11	373.4	358.3	15.1
U12	429.7	408.3	21.4	D12	427.4	408.1	19.3
U13	390.4	371.1	19.3	D13	386.7	339.5	17.2
U14	410.5	390.8	19.7	D14	410.7	393.4	17.3
U15	362.5	346.4	16.1	D15	392.1	373.8	18.3
U16	421.7	398.3	23.4	D16	400.1	383.3	16.8
U17	397.6	372.1	25.5	D17	321.5	299.5	22
U18	374.1	355.8	18.3	D18	392.2	3711.9	20.3
U19	470.3	445.9	24.4	D19	401.6	383.2	18.4
U20	313.8	295.1	18.7	D20	391.3	368.5	22.8
U21	401.3	371.4	29.9	D21	385.6	361.5	24.1
U22	418.2	387.5	30.7	D22	400.5	375.2	25.3
U23	378.3	345.6	32.7	D23	328.3	298.6	29.7
U24	391.5	357.5	34	D24	418.4	382.5	35.9
U25	413.5	379.7	33.8	D25	380.3	341.1	39.2
U26	383.2	337.3	45.9	D26	385.5	338.6	46.9
U27	461.6	413.8	47.8	D27	372.5	325.5	47
U28	329.3	277.4	51.9	D28	394.7	342.3	52.4
U29	382.3	323.5	58.8	D29	382.7	331.4	51.3
U30	438.5	332.3	106.2	D30	383.2	309.5	73.7
U31	447.5	353.6	93.9	D31	396.1	314.7	81.4
U32	366.1	308.5	57.6	D32	414.3	355.3	59
U33	385.3	335.8	49.5	D33	415.3	359.2	56.1
U34	352.3	305.1	47.2	D34	353.5	299.4	54.1
U35	391.4	358.4	33	D35	392.5	356.7	35.8
U36	385.2	353.4	31.8	D36	370.2	337.5	32.7
U37	371.9	342.1	29.8	D37	292.9	263.5	29.4
U38	367.5	343.1	24.4	D38	402.4	375.3	27.1
U39	378.3	356.5	21.8	D39	408.3	388.1	20.2
U40	355.9	336.8	19.1	D40	303.5	305.7	−2.2
U41	378.7	359.5	19.2	D41	321.3	308.2	13.1
U42	357.3	370.7	−13.4	D42	390.7	375.5	15.2
U43	402.5	391.3	11.2	D43	404.3	391.7	12.6

Table 3: Continued.

Boom no.	Regularly detected measured value	Actual value of handover acceptance	D value	Boom no.	Regularly detected measured value	Actual value of handover acceptance	D value
U44	331.4	315.4	16	D44	347.5	329.3	18.2
U45	427.3	404.5	22.8	D45	363.3	348.9	14.4
U46	375.3	359.5	15.8	D46	391.1	379.1	12
U47	398.5	387.1	11.4	D47	418.6	400.4	18.2
U48	336.7	330.5	6.2	D48	354.3	339.6	14.7
U49	402.8	404	−1.2	D49	374.7	361.2	13.5
U50	363.2	339.3	23.9	D50	397.8	378.8	19
U51	411.5	393.4	18.1	D51	366.9	345.5	21.4
U52	360.3	347.8	12.5	D52	414.1	397.5	16.6
U53	382.3	358.4	23.9	D53	370.9	350.9	20
U54	398.1	376.5	21.6	D54	404.8	393.6	11.2
U55	365.8	358.3	7.5	D55	358.1	348.3	9.8
U56	413.6	397.9	15.7	D56	396.7	382.5	14.2
U57	356.7	346.3	10.4	D57	354.4	342.7	11.7
U58	398.5	385.4	13.1	D58	384.4	371.8	12.6
U59	407.2	391.1	16.1	D59	396.3	381.4	14.9
U60	368.4	349.7	18.7	D60	359.2	343.9	15.3

Table 4: Calculation results of internal forces of main arch ribs under dead load.

Control section	Axial force (kN)		Bending moment (kN·m)		Deflection (mm)	
	Calculation I	Calculation II	Calculation I	Calculation II	Calculation I	Calculation II
Arch foot	44132	43986	−44891	−43527	0	0
L/4 section (top chord)	17789	17861	27	27	65	63
L/4 section (bottom chord)	16758	16903	151	162	65	63
L/2 section (top chord)	17137	17242	274	279	107	103
L/2 section (bottom chord)	14459	14584	315	308	107	103

At the same time, according to the network weight value w_{ij} and threshold to be optimized θ, the key parameters in the fireworks algorithm are set as follows: population size $n = 70$, firework explosion radius adjustment constant $d = 5$, firework explosion spark number adjustment constant $c = 40$, upper limit of firework explosion spark number $ub = 0.8$, lower limit of firework explosion spark number $lb = 0.04$, Gaussian variation spark number $g = 5$, and maximum iteration times $T = 1000$.

5.2. Experimental Results and Performance Analysis of Prediction Model. The internal force and deformation of the arch rib control section under dead load calculated by the model in this paper are shown in Table 4.

In Table 4, Calculation I is the calculation result of the testing agency, and Calculation II is the calculation result of the model in this article; the axial force in the table is positive with pressure; the side tension below the bending moment is positive; the deflection is positive downward.

The comparison between the cable force calculated by the model in this article and the detection mechanism and the measured cable force is shown in Table 5, taking the cable force of the upstream suspender as an example.

In Table 5, Calculation I is the calculation result of the testing agency, and Calculation II is the calculation result of the model in this article. Difference ① = Calculate the mean value of II − Calculate I, with an increase in the difference being positive and a decrease being negative, and a percentage of difference ① = Difference ①/Calculate I. Difference ② = calculated II mean − measured mean, if the calculated II mean is greater than the measured mean, it is positive, and if it is less than the measured mean, it is negative, and a percentage of difference ② = difference ②/measured mean.

From Tables 4 and 5, it can be seen that the axial force calculation results of the model and the detection mechanism in this paper are very similar under the dead load, the bending moment calculation results of each section are basically consistent, and the deflection calculation results are also basically similar. The maximum deviation between the upstream suspender cable force calculated by this model and the cable force calculated by the detection mechanism is 5.5%, and the maximum deviation from the measured cable force is 5.6%. Therefore, the calculation results of this model are reliable and can be used as the basis for further analysis and research.

5.3. Suspender Damage Calculation Prediction. Arch ribs, transverse connections, and suspension structures are the general components of the span structure of half-through arch bridge and through arch bridges. The suspender is composed of load-bearing steel wire and steel pipe sheathed outside it, which plays a key role in hanging the bridge deck. The waterproof system of its upper and lower anchor heads is easy to age. Among the components of the arch bridge, the suspender is the most easily damaged component, so the research on damage identification of this kind of arch bridge should focus on the suspender health detection. Taking No. 30 suspender in the middle as an example, some training samples are listed in Tables 6 and 7.

Firstly, the 0-1 standardization strategy according to equation (15) in Section 4.2 is used to standardize the experimental data, and then the experimental dataset is established with the standardized data to train and test the FWA-BP neural network prediction model. The first 80% of the data in the experimental dataset is selected as the training data set, and the last 20% of the data in the dataset is selected as the test dataset. The prediction model based on FWA-BP neural network proposed in this paper is tested and verified.

Secondly, to further verify the prediction performance based on FWA-BP neural network, the same datasets are used to train the traditional BP neural network, genetic algorithm-improved BP neural network (GA-BPNN), and particle swarm optimization algorithm-improved BP neural network (PSO-BPNN). The parameter setting of the GA is as follows: population size popu = 30, genetic algebra gen = 100, crossover probability pcross = 0.8, and mutation probability pmutation = 0.05. For PSO algorithm, the parameters are as follows: speed update parameter $c_1 = c_2 = 1.49445$, evolution times maxgen = 150, population size sizepop = 30, individual maximum $pop_{max} = 7$, individual minimum $pop_{min} = -7$, individual maximum speed v_{max}, and individual minimum speed v_{min}. The parameters of BP neural network in BP neural network prediction model optimized by different algorithms are the same as those in FWA-BP neural network model described in Section 4.2.

Thirdly, to reduce the accidental factors in the experimental process, the same algorithm model is trained and tested for 3 times with the same data, and the average value of the prediction error and iteration time of 3 times are taken as the prediction error and iteration times of the algorithm. Specifically, under the same experimental conditions, the GA-BP neural network and PSO-BP neural network models are simulated, and the prediction results of the neural network prediction models optimized by different algorithms are obtained. The results are shown in Tables 8 and 9.

Table 5: Comparison between the calculated and measured cable forces of the suspender (unit: kN).

Hanger no.	Calculation I	Calculation II	Calculation II mean value	Measured value	Measured mean value	Difference value ①	Difference ① percentage (%)	Difference value ②	Difference ② percentage (%)
U1	390.4	355.8	393.5	369.4	396	3.1	0.8	−2.5	−0.6
U2		431.3		422.6					
U3	381.1	380.2	378.9	391.3	380.9	−2.2	−0.6	−2	−0.5
U4		377.7		370.5					
U5	379.7	383.8	384.4	403.9	385.7	4.7	1.2	−1.3	−0.3
U6		384.7		367.4					
U7	391.2	389.7	390.1	492.3	392	−1.1	−0.3	−1.9	−0.5
U8		390.4		291.6					
U9	375.3	387.5	388.4	416.1	393.7	13.1	3.5	−5.3	−1.3
U10		389.3		371.3					
U11	389.1	385.4	386.1	388.5	409.1	−3	−0.8	−23	−5.6
U12		386.7		429.7					
U13	381.9	387.6	387.9	390.4	400.5	6	1.6	−12.6	−3.1
U14		388.1		410.5					
U15	376.8	386.5	386.9	362.5	392.1	10.1	2.7	−5.2	−1.3
U16		387.3		421.7					
U17	383.6	389.7	389.2	397.6	385.9	5.6	1.5	3.3	0.9
U18		388.6		374.1					
U19	380.9	387.5	387.7	470.3	392.1	6.8	1.8	−4.4	−1.1
U20		387.8		313.8					
U21	380.6	387.8	387.6	401.3	409.8	7	1.8	−22.2	−5.4
U22		387.3		418.2					
U23	382.5	388.6	388.4	378.3	384.9	5.9	1.5	3.5	0.9
U24		388.1		391.5					
U25	384.7	388.6	388.8	413.5	398.4	4.1	1.1	−9.6	−2.4
U26		388.9		383.2					
U27	381.9	388.5	388.6	461.6	395.5	6.7	1.8	−6.9	−1.7
U28		388.7		329.3					
U29	386.5	389.9	390.2	382.3	410.4	3.7	1.0	−20.2	−4.9
U30		390.4		438.5					
U31	379.9	386.6	387	447.5	406.8	7.1	1.9	−19.8	−4.9
U32		387.4		366.1					
U33	378.3	388.7	388.8	385.3	368.8	10.5	2.8	20	5.4
U34		388.9		352.3					
U35	385.6	388.4	388.7	391.4	388.3	3.1	0.8	0.4	0.1
U36		388.9		385.2					
U37	379.4	388.3	388.5	371.9	369.7	9.1	2.4	18.8	5.1
U38		388.6		367.5					
U39	377.1	386.3	386.6	378.3	367.1	9.5	2.5	19.5	5.3
U40		386.8		355.9					
U41	371.6	379.1	380.3	378.7	368	8.7	2.3	12.3	3.3
U42		381.4		357.3					
U43	376.4	385.5	386.4	402.5	367	10	2.7	19.4	5.3
U44		387.2		331.4					
U45	388.7	389.1	389	427.3	401.3	0.7	0.2	−12.3	−3.1
U46		388.9		375.3					
U47	383.3	386.9	386.8	398.5	367.6	3.5	0.9	19.2	5.2
U48		386.7		336.7					
U49	372.4	387.4	387.5	402.8	383	15.1	4.1	4.5	1.2
U50		387.6		363.2					
U51	392.1	387.6	387.5	411.5	385.9	−4.6	−1.2	1.6	0.4
U52		387.2		360.3					
U53	367.9	387.7	388.1	382.3	390.2	20.2	5.5	−2.1	−0.5
U54		388.5		398.1					
U55	378.6	384.6	384.2	365.8	389.7	5.6	1.5	−5.5	−1.4
U56		383.8		413.6					
U57	383.3	378.1	379.2	356.7	377.6	−4.1	−1.1	1.6	0.4
U58		380.4		398.5					
U59	391.5	431.7	393.8	407.2	387.8	2.3	0.6	6.0	1.5
U60		356		368.4					

Table 6: Part of damage training sample data of No. 30 unit (I).

Node	Damage degree					
	10%	20%	30%	40%	50%	59%
1	0	0	0	0	0	0
2	0	0	0.1662	0.1702	0.1667	91.275
3	0	0	0.3515	0.3531	0.3625	158.625
4	0	0	0.1664	0.3533	0.3675	216.791
5	0	0	0.1665	0.1659	0	264.95
6	0	0.1661	0	0.1705	0	290.175
7	0.1669	0.1663	0.1663	0	0	321.0266
8	0.1667	0	0	0.1767	0	317.34
9	0.0824	0.0571	0.043	0.0433	0.2524	261.84
10	0.0826	0.0727	0.0731	0.0855	0.0525	211.28
11	0.1042	0.1917	0.138	0.141	0.1506	153.583
12	0.1041	0.2073	0	0	0.235	91.333
13	0.1664	0.1765	0	0.1672	0	13.41
14	0.3323	0.5691	0.4791	0.739	0.8825	131.053
15	0.1658	0	0.1665	0.5685	0.775	197.6223
16	0.1601	0.5689	0.9577	2.55	2.175	328.271
17	7.4573	16.5638	26.1535	39.5231	58.6427	698.4525
18	8.1509	17.0935	27.8201	40.9312	60.0525	701.3361
19	16.537	38.0311	66.742	103.198	145.995	2379.856
20	17.055	40.3413	68.957	105.773	146.894	2415.182
21	18.543	41.7536	69.065	107.561	148.863	2568.675
22	19.145	42.7431	71.653	108.973	150.678	2605.412
23	20.973	43.7159	72.132	110.374	152.896	2689.325
24	21.315	44.4381	73.035	112.875	153.787	2701.188
25	22.045	44.983	73.958	118.053	157.329	2798.237
26	22.813	45.162	74.345	119.765	158.995	2835.889
27	28.549	56.461	85.842	211.537	173.139	2904.647
28	29.735	57.885	86.982	213.987	173.568	2981.427
29	38.941	68.125	91.413	223.614	223.854	3135.532
30	64.37	138.1	201.973	325.705	578.1125	637.1875
31	62.81	136.47	198.149	323.436	574.672	638.4538
32	39.076	71.3125	95.787	141.314	213.424	2144.7475
33	28.876	59.427	89.288	135.4134	189.413	1943.3546
34	27.971	58.546	87.537	133.612	187.375	1913.5632
35	23.897	53,995	83.749	118.414	175.441	1854.574
36	22.769	52.895	82.564	117.142	173.982	1832.127
37	21.4523	49.375	79.845	95.1575	164.7813	1722.427
38	20.6345	48.174	78.541	93.825	163.3574	1701.132
39	19.0528	46.982	76.564	91.413	161.7462	1690.545
40	18.9541	47.036	75.635	91.854	161.3421	1663.213
41	17.3425	45.758	74.138	90.751	159.876	1589.527
42	16.9547	43.325	73.062	87.054	158.645	1561.172
43	8.5612	18.095	32.797	42.1312	66.0937	1345.3341
44	7.9893	17.113	31.942	41.5752	65.7401	1297.5425
45	0.1678	0.5524	1.0875	2.1541	4.5425	345.2674
46	0.1794	0	0.1673	0.5327	0.8625	254.4452
47	0.3795	0.5674	0.6887	0.7975	0.9812	102.425
48	0.1673	0.1792	0	0.2425	0	13.5547
49	0.1054	0.1898	0	0	0.2525	91.2654
50	0.1045	0.1819	0.225	0.2251	0.2506	139.4425
51	0.08703	0.0726	0.0798	0.0825	0.0235	209.3234
52	0.087	0.0643	0.0411	0.0621	0.4354	253.4349
53	0.1701	0	0	0.2674	0	287.7556
54	0.1676	0.1675	0.1662	0	0	305.4553
55	0	0.1673	0	0.2452	0	285.2242
56	0	0	0.1673	0.2519	0	256.3345
57	0	0	0.1662	0.4425	0.4312	223.1525
58	0	0	0.4197	0.4509	0.4411	167.3255
59	0	0	0.1659	0.1734	0.1741	87.5254
60	0	0	0	0	0	0

Table 7: Part of damage training sample data of No. 30 unit (II).

Node	Damage degree				
	60%	65%	70%	80%	90%
1	0	0	0	0	0
2	79.1347	45.845	0.3424	0.3522	0.7453
3	147.2254	134.4649	0	0	0.6133
4	197.5565	175.6746	0.3245	0.5252	0.9585
5	249.2275	235.754	0	0	0.9356
6	268.1325	298.545	0.5345	0.3525	0.9456
7	326.1245	375.4342	0	0.3423	0.7455
8	311.4431	401.6757	0.3532	0	0.6465
9	279.8125	386.432	0.1452	0.1324	0.1342
10	241.1275	378.042	0.3432	0.2964	0.4653
11	126.5763	279.4345	0.1421	0.3765	0.3523
12	91.1134	187.6223	0.1432	0.1976	5.5474
13	13.4435	96.2275	0	0.3545	4.3635
14	132.3357	9.7567	1.7474	4.3534	15.463
15	154.0027	99.4325	1.3545	3.3536	307.643
16	403.5587	189.3322	5.3463	7.35335	875.453
17	740.7863	265.785	98.674	111.7845	2151.785
18	741.6259	263.522	97.252	112.6456	2142.452
19	2069.896	348.7963	210.1742	278.562	1905.7853
20	2075.953	350.0856	209.6561	279.985	1890.5643
21	2089.786	349.8963	212.4539	277.962	1881.0874
22	2103.615	351.5428	217.9865	280.785	1865.9085
23	2155.456	354.4425	223.3422	285.433	1843.5244
24	2298.5631	396.67	289.455	365.8965	1792.786
25	2367.7535	407.86	296.754	373.6578	1743.523
26	2591.762	447.6751	318.895	451.893	1658.9851
27	2678.525	456.8423	326.336	464.556	1634.3323
28	2815.675	562.753	358.952	512.753	1583.897
29	2956.544	576.352	365.43	534.564	1565.346
30	643.4632	681.2245	874.532	1354.433	855.895
31	651.5453	667.5531	858.761	1342.765	871.547
32	2145.5643	624.335	366.546	535.432	1567.548
33	2137.8356	615.975	359.354	528.653	1552.657
34	2005.633	603.3634	328.675	456.744	1636.463
35	1998.761	594.7641	321.879	437.563	1689.674
36	1979.742	535.436	301.345	374.5742	1745.363
37	1865.675	525.653	298.615	365.6751	1794.788
38	1636.502	517.543	243.346	289.766	1854.634
39	1601.893	512.012	239.879	280.184	1873.172
40	1597.981	509.675	231.783	277.892	1883.525
41	1569.785	504.156	227.533	275.173	1892.782
42	1559.247	502.873	221.875	276.845	1906.783
43	1386.4654	496.7678	94.4563	123.441	2143.111
44	1375.6751	495.8964	95.8915	125.896	2150.782
45	354.4453	455.8687	5.3563	7.34653	874.533
46	296.9672	324.5235	1.3452	3.56456	305.252
47	134.0528	231.745	1.7545	4.63663	15.3252
48	31.523	134.4425	0	0.3542	4.3523
49	69.525	21.452	0.14523	0.1342	5.4534
50	141.845	86.2452	0.14565	0.3525	0.3432
51	225.5434	154.5422	0.3523	0.2425	0.46467
52	278.3548	196.1132	0.1342	0.1235	0.1542
53	307.959	234.3321	0.3532	0	0.6356
54	355.4564	254.4254	0	0.3523	0.7363
55	313.453	313.553	0.5765	0.3453	0.9546
56	276.5635	276.5459	0	0	0.9353
57	225.5257	234.442	0.3235	0.5754	0.9457
58	175.5677	152.342	0	0	0.6363
59	104.7459	112.434	0.3543	0.3634	0.7546
60	0	0	0	0	0

Table 8: Prediction results of damage degree based on different models.

Output target value	Prediction result			
	BPNN	GA-BPNN	PSO-BPNN	FWA-BPNN
0.21	0.2011	0.2057	0.2069	0.2074
0.35	0.3381	0.3452	0.3473	0.3489
0.42	0.4019	0.4096	0.4125	0.4138
0.54	0.5237	0.5365	0.5349	0.5372
0.63	0.6078	0.6253	0.6234	0.6281
0.76	0.7326	0.7488	0.7502	0.7535
0.87	0.8469	0.8674	0.8671	0.8682
0.98	0.9575	0.9706	0.9713	0.9716

Table 9: Prediction results of each model for comparative analysis.

Test no.	Model	AE (%)	AE_{max} (%)	R	T/s
1	BPNN	5.74	20.81	0.902	60.49
	GA-BPNN	4.26	13.26	0.948	52.36
	PSO-BPNN	4.03	13.19	0.959	51.42
	FWA-BPNN	3.59	9.79	0.963	51.73
2	BPNN	5.62	22.35	0.913	59.16
	GA-BPNN	4.11	12.79	0.962	43.69
	PSO-BPNN	3.98	11.36	0.969	42.58
	FWA-BPNN	3.24	9.14	0.975	40.48
3	BPNN	5.49	20.10	0.926	51.38
	GA-BPNN	3.83	11.51	0.964	41.67
	PSO-BPNN	3.72	11.34	0.973	41.09
	FWA-BPNN	3.07	8.82	0.982	40.16

It can be seen from Tables 8 and 9 that in the three rounds of tests, the average relative error AE, maximum relative error AE_{max}, similarity R, and single round cumulative time T are predicted by each model, and the prediction results of BP neural network optimized by different algorithms fluctuate in different test samples. However, on the whole, the error rate of the prediction model based on FWA-BP neural network is lower than that of the existing prediction models based on PSO-BP neural network and GA-BP neural network, and its results are closer to target values than the other models.

6. Conclusions

In view of the weak generalization ability and low prediction accuracy of the prediction model based on the traditional BP neural network, the fireworks algorithm is introduced into the BP neural network, and the weights and thresholds of the BP neural network are optimized and improved with the help of the fireworks algorithm. A prediction model based on the fireworks algorithm-improved BP neural network (FWA-BP) is proposed, and the algorithm of the prediction model based on FWA-BP neural network is implemented. Then, taking the damage prediction of long-span arch bridge as an example, the damage prediction model based on FWA-BP neural network is established, and the performance of damage prediction is simulated and tested. Compared with the prediction methods based on BP neural network, GA-BP neural network, and PSO-BP neural network, the results show that under the given training target value, the prediction method based on FWA-BP neural network proposed in this paper has smaller prediction error rate and fewer iterations, which can effectively improve the prediction performance of BP neural network. Therefore, the damage degree prediction method of long-span arch bridge proposed in this paper is feasible and provides a theoretical basis for related engineering research.

Data Availability

The data used to support the findings of this study are included within the article.

Conflicts of Interest

The authors declare that there are no conflicts of interest regarding the publication of this paper.

Acknowledgments

The authors appreciate the financial support from the Heilongjiang Province Government of China and acknowledge the technical support from the bridge design and construction enterprises for this work. This research was supported by the Special Research Project of Basic Business in Colleges and Universities (grant nos. 135509212 and 145209147) and Provincial Platform Opening Project of Heilongjiang Province of China (grant no. WNCGQJKF202101).

References

[1] J. P. Shu, Z. Y. Zhang, I. Gonzalez, and R. Karoumi, "The application of a damage detection method using Artificial Neural Network and train-induced vibrations on a simplified railway bridge model," *Engineering Structures*, vol. 52, pp. 408–421, 2013.

[2] Y. S. Ma, Y. F. Wang, L. Su, and S. Q. Mei, "Influence of creep on dynamic behavior of concrete filled steel tube arch bridges," *Steel and Composite Structures*, vol. 21, no. 1, pp. 109–122, 2016.

[3] X. L. Xu, K. W. Shi, X. H. Li, Z. J. Li, R. G. Wang, and Y. W. Chen, "Optimization analysis method of new orthotropic steel deck based on backpropagation neural network-simulated annealing algorithm," *Advances in Civil Engineering*, vol. 2021, Article ID 8888168, 16 pages, 2021.

[4] Z. Y. Xia, S. T. Quek, A. Q. Li et al., "Sensitivity analysis in seismic reliability of an urban self-anchored suspension bridge," *Mechanical Systems and Signal Processing*, vol. 164, Article ID 108231, 2022.

[5] J. Yuan, S. T. Lv, X. H. Peng, L. Y. You, and M. Borges Cabrera, "Investigation of strength and fatigue life of rubber asphalt mixture," *Materials*, vol. 13, no. 15, p. 3325, 2020.

[6] C. X. Li and J. H. Li, "Support vector machines approach to conditional simulation of non-Gaussian stochastic process," *Journal of Computing in Civil Engineering*, vol. 26, no. 1, pp. 131–140, 2012.

[7] H. B. Hwarng, "Insights into neural-network forecasting of time series corresponding to ARMA structures," *Omega*, vol. 29, no. 3, pp. 273–289, 2001.

[8] H. Q. Mu, Z. J. Zheng, X. H. Wu, and C. Su, "Bayesian network-based modal frequency-multiple environmental factors pattern recognition for the Xinguang Bridge using long-term monitoring data," *Journal of Low Frequency Noise, Vibration and Active Control*, vol. 39, no. 3, pp. 545–559, 2020.

[9] P. Zhang, H. N. Wu, R. P. Chen, and T. H. T. Chan, "Hybrid meta-heuristic and machine learning algorithms for tunneling-induced settlement prediction: a comparative study," *Tunnelling and Underground Space Technology*, vol. 99, Article ID 103383, 2020.

[10] M. Lu, S. M. AbouRizk, and U. H. Hermann, "Sensitivity analysis of neural networks in spool fabrication productivity studies," *Journal of Computing in Civil Engineering*, vol. 15, no. 4, pp. 299–308, 2001.

[11] Y. Sun, Q. H. Jiang, T. Yin, and C. B. Zhou, "A back-analysis method using an intelligent multi objective optimization for predicting slope deformation induced by excavation," *Engineering Geology*, vol. 239, pp. 214–228, 2018.

[12] Y. Cao, Y. Zandi, A. S. Agdas et al., "A review study of application of artificial intelligence in construction management and composite beams," *Steel and Composite Structures*, vol. 39, no. 6, pp. 685–700, 2021.

[13] X. Fang, H. Luo, and J. Tang, "Structural damage detection using neural network with learning rate improvement," *Computers and Structures*, vol. 83, no. 25-26, pp. 2150–2161, 2005.

[14] G. B. Zhang, C. F. Chen, Y. H. Zhang, H. C. Zhang, Y. F. Wang, and X. Y. Wang, "Optimised neural network prediction of interface bond strength for GFRP tendon reinforced cemented soil," *Geomechanics And Engineering*, vol. 28, no. 6, pp. 599–611, 2022.

[15] M. Su, H. Peng, and S. F. Li, "Application of an interpretable artificial neural network to predict the interface strength of a near-surface mounted fiber-reinforced polymer to concrete joint," *Journal of Zhejiang University Science*, vol. 22, no. 6, pp. 427–440, 2021.

[16] M. A. Mashrei, R. Seracino, and M. S. Rahman, "Application of artificial neural networks to predict the bond strength of FRP-to-concrete joints," *Construction and Building Materials*, vol. 40, pp. 812–821, 2013.

[17] J. A. Abdalla, A. Elsanosi, and A. Abdelwahab, "Modeling and simulation of shear resistance of R/C beams using artificial neural network," *Journal of the Franklin Institute*, vol. 344, no. 5, pp. 741–756, 2007.

[18] Z. Waszczyszyn and L. Ziemianski, "Neural networks in mechanics of structures and materials new results and prospects of applications," *Computers and Structures*, vol. 79, no. 22-25, pp. 2261–2276, 2001.

[19] L. Wang, Y. Zeng, and T. Chen, "Back propagation neural network with adaptive differential evolution algorithm for time series forecasting," *Expert Systems with Applications*, vol. 42, no. 2, pp. 855–863, 2015.

[20] B. Han, F. Geng, S. Dai, G. Y. Gan, S. L. Liu, and L. H. Yao, "Statistically optimized back-propagation neural-network model and its application for deformation monitoring and prediction of concrete-face rockfill dams," *Journal of Performance of Constructed Facilities*, vol. 34, no. 4, 2020.

[21] Z. J. Li, G. Y. Kan, C. Yao, Z. Y. Liu, Q. L. Li, and S. Yu, "Improved neural network model and its application in hydrological simulation," *Journal of Hydrologic Engineering*, vol. 19, no. 10, 2014.

[22] H. Dongmei, H. Shiqing, H. Xuhui, and Z. Xue, "Prediction of wind loads on high-rise building using a BP neural network combined with POD," *Journal of Wind Engineering and Industrial Aerodynamics*, vol. 170, pp. 1–17, 2017.

[23] Z. X. Yue, Y. L. Ding, H. W. Zhao, and Z. W. Wang, "Case study of deep learning model of temperature-induced deflection of a cable-stayed bridge driven by data knowledge," *Symmetry*, vol. 13, no. 12, p. 2293, 2021.

[24] F. L. Kuang, Z. L. Long, D. M. Kuang, X. W. Liu, and R. Q. Guo, "Application of back propagation neural network to the modeling of slump and compressive strength of composite geopolymers," *Computational Materials Science*, vol. 206, Article ID 111241, 2022.

[25] G. W. Chen, W. C. Tang, S. Chen, S. Y. Wang, and H. Z. Cui, "Prediction of self-healing of engineered cementitious composite using machine learning approaches," *Applied Sciences*, vol. 12, no. 7, p. 3605, 2022.

[26] J. Luo, R. Ren, and K. D. Guo, "The deformation monitoring of foundation pit by back propagation neural network and genetic algorithm and its application in geotechnical engineering," *PLoS One*, vol. 15, no. 7, Article ID e0233398, 2020.

[27] C. Hou and X. G. Zhou, "Strength prediction of circular CFST columns through advanced machine learning methods," *Journal of Building Engineering*, vol. 51, Article ID 104289, 2022.

[28] Y. Tan and Y. C. Zhu, "Fireworks Algorithm for Optimization Lecture Notes in Computer Science," in *Proceedings of the International Conference on Swarm Intelligence ICSI 2010*, pp. 355–364, Springer, Beijing, China, June 2010.